1

Porous Construction Materials: Characterizations and Modeling

This chapter presents experimental methods and some modeling of microstructural properties of porous media, mainly applied to construction materials. The methods shown are generally recommended by some specialized users or by standards. Some models shown are based on the microstructural properties of the medium, while others describe simulated microstructures built numerically based on experimental data, such as porosity, tortuosity and connectivity, and on the hydration process in the particular case of cementitious materials.

In the final section of the chapter, the microstructural properties of a porous medium are linked to a transfer property, namely intrinsic permeability. For this purpose, several approaches are presented: calculation of the permeability from data on the pore structure (e.g. distribution of pore radii) and calculation from 3D constructed microstructures.

1.1. Definition of porous media

A porous medium is composed of a rigid solid matrix, or with low deformation, and of a void network. The porosity, denoted as ε_p in the

---

Chapter written by Abdelkarim AÏT-MOKHTAR, Ameur HAMAMI, Philippe TURCRY and Ouali AMIRI.

following, is expressed by the ratio of the void phase volume and the total volume of the medium (equation [1.1]):

$$\varepsilon_P = \frac{V_{Voids}}{V_{total}} \qquad [1.1]$$

The pores (Figure 1.1) can be connected and cross the medium from side to side. In this case, the pore structure is known as “percolating”. Trapped gaps or blind pores can also be found within the medium.

Figure 1.1. *Porosity: ① Percolation/connected porosity, ② Trapped gap, ③ Blind pore*

A lot of construction materials are porous. The pore structure, i.e. porosity and pore size and shape, depends, of course, on the type of the material. The porosity of construction materials is the place where transfer phenomena occur. These phenomena are affected by microstructural parameters, such as pore size distribution or connectivity. Generally speaking, it is necessary to consider all these parameters in order to study the transfer properties. For instance, the most porous material is not necessarily the most permeable material: pore size also affects the transfer by permeation.

From this point of view, two relevant microstructural parameters are usually used to characterize the pore structure: tortuosity and constrictivity. The tortuosity (τ) quantifies the elongation of the transfer path due to pore geometry, as shown in Figure 1.2(a).

Usually, tortuosity (equation [1.2]) is calculated as the ratio of the average pore length and the sample thickness. The tortuosity models the average transfer path through the material:

$$\tau = \frac{l}{l_0} \tag{1.2}$$

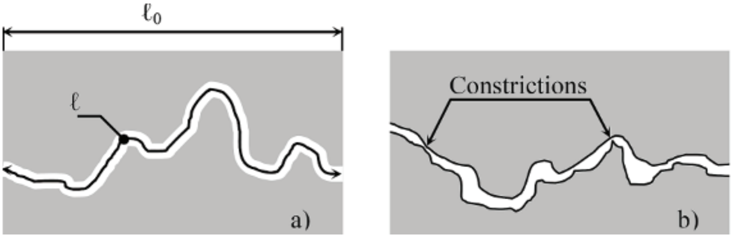

Figure 1.2. *Microstructural parameters: a) tortuosity and b) constrictivity*

The constrictivity (δ) (Figure 1.2(b)) consists of a reduction of the pore size along the pore. It reflects the fact that the pore section is not uniform but undergoes several constrictions that affect the transfer phenomena.

1.2. Different experimental tools for the characterization of porous materials

The transfer of chemical species in a porous medium is closely related to the porous microstructure [OLL 92]. Thus, its characterization is required to study the structure's durability. The knowledge of parameters such as porosity or pore-specific areas is necessary for the investigation of the physicochemical phenomena involved during mass exchanges between the wall of the pore and the pore solution interface inside the medium, which governs boundary conditions in the study of mass transfer.

1.2.1. *Measurements of porosity*

The main direct methods of porosity measurements in construction materials are water porosimetry and mercury intrusion porosimetry (MIP). These two methods are described hereafter. In the case of cementitious materials, recommended protocols exist, particularly in France [AFP 97, ARL 07].

1.2.1.1. *Water porosimetry*

Generally, the water porosimetry test is carried out according to the procedure recommended by the French association AFREM (*Association Française de Recherche et d'Essais sur les Matériaux et les Constructions,* French Association for the Research and Testing of Materials and Structures) [AFP 97] and the standard NF P18-459 [AFN 10]. The samples are first water-saturated with distilled water under vacuum at a saturation vapor pressure of 18 mmHg in order to obtain the saturated mass m_{sat}. The sample volumes V_{tot} are then determined from buoyancy weighing. Finally, samples are dried at a temperature between 60 and 105°C until mass stabilization to obtain the dried mass m_{dry}. The mass stabilization is obtained when the relative mass loss in 24 h is less than 0.05%. The porosity ε_p is calculated using equation [1.3]:

$$\varepsilon_p = \frac{m_{sat} - m_{dry}}{\rho_w . V_{total}} \times 100 \ (\%) \qquad [1.3]$$

where ρ_w is the density of water.

1.2.1.2. *Mercury intrusion porosimetry*

The MIP test is carried out by injecting mercury through a porous medium sample of 1–2 cm^3 placed under vacuum in a penetrometer. This injection is performed by varying the injection pressure P, which can reach more than 400 MPa, so that the mercury penetrates pores whose diameters D are between 0.003 and 360 µm. Each pressure increment permits the calculation of the diameter of the pores filled with a volume of mercury V_{Hg} according to the Laplace's law (equation [1.4]). The principle of measurement is schematized in Figure 1.3:

$$D = \frac{4\gamma\cos\theta}{P} \qquad [1.4]$$

where γ is the surface tension between the pore surface and the mercury (N/m). This parameter varies with the purity of mercury. The value usually used is 0.485 N/m. θ is the contact angle in degree between the mercury meniscus and the pore wall. The usual value for this parameter is 130°.

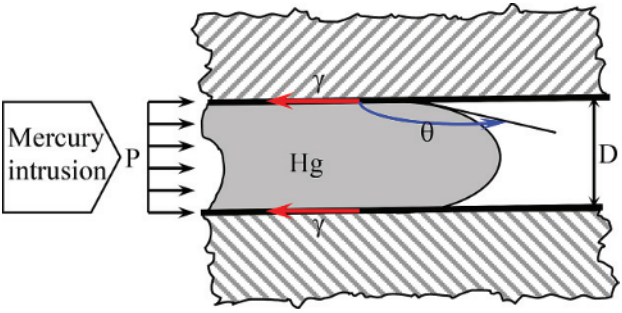

Figure 1.3. *Schematic view of the MIP principle. For a color version of the figure, see www.iste.co.uk/ait-mokhtar/coastal.zip*

At the end of the test, a pore size distribution of the porous network is obtained. The latter is given by a plot of the differential log of the mercury volume intrusion versus the pore diameter. Figure 1.4 gives an example of a result obtained by this method. The specific area of the material can also be calculated from the collected data.

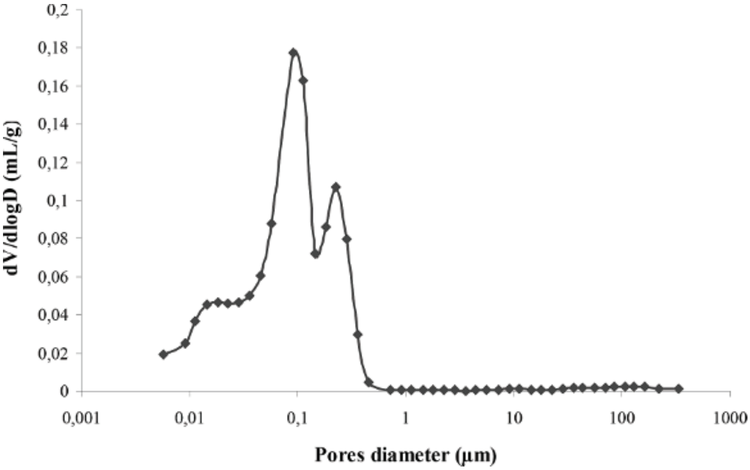

Figure 1.4. *Example of pore size distribution obtained by MIP on a mortar with W/C = 0.6 [HAM 09]*

The MIP is a measurement technique widely used to characterize a porous material. It gives a simplified representation of the microstructure of the material because the pores are assumed to be cylindrical. Moreover, this method facilitates only the determination of the pore entrance diameter. As shown in Figure 1.5, large pores located after smaller ones cannot be detected by the MIP method, because the required pressure to fill the larger pores is the same than that necessary for penetrating the smallest ones (this phenomenon is commonly called “ink-bottle” effect) [DIA 00].

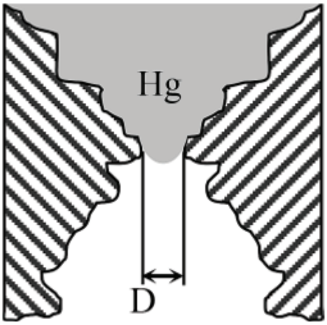

Figure 1.5. *Pore diameter measured by MIP*

Despite these assumptions and approximation, the MIP technique remains one of the main tools used for the characterization of porous materials.

1.2.2. *Pore size distribution by sorption/desorption isotherms*

The water vapor sorption/desorption isotherm gives the evolution of the water content of a porous material as a function of the ambience relative humidity (RH) at constant temperature. For each RH, it is possible to determine a pore diameter *D* that is filled with water. A pore size distribution is obtained for a range of RH. For this purpose, the Kelvin–Laplace law, given in equation [1.5], is used to calculate the pore diameter:

$$D = -\frac{4M_v\gamma_{aw}}{\rho_{aw}RT\ln(RH)} \quad [1.5]$$

where M_v is the molar mass of the water vapor (18 g/mol), γ_{aw} is the surface tension of the liquid water (equal to 0.07275 $N.m^{-1}$ at 20°C), ρ_w is the mass density of liquid water and R is the ideal gas constant (8.314 $J.K^{-1}.mol^{-1}$).

The pore diameters obtained by this technique are located between 0.6 and 35 nm for an RH range between 3 and 94%.

The measurement of sorption/desorption isotherms can also be carried out by using a gas such as nitrogen. This method consists in measuring the amount of nitrogen molecules adsorbed by the material under a constant temperature of 77 K. This technique is based on the works of Brunauer *et al.* [BRU 38], which is commonly known as the Brunauer–Emmett–Teller (BET) technique. The latter makes the determination of the specific area of a solid possible, the pore size distribution that can reach pore with a diameter smaller than 200 nm. This pore size distribution is based on the step-by-step analysis of the sorption/desorption isotherms following the Barrett–Joyner–Halenda (BJH) method [BAR 51].

1.2.3. *Characterization of pore structure by NMR*

The application of nuclear magnetic resonance (NMR) for the characterization of pore structure is an attractive method [PLA 01]. Contrary to intrusion methods, it is fully non-destructive and does not require sample preparation such as drying, liquid saturation or polishing.

In a material, any nucleus with a spin (i.e. nucleus with an odd number of protons) shows an intrinsic magnetic moment. When the material is immersed in an intense magnetic field, classically denoted as $\overrightarrow{B_0}$, it becomes magnetized due to the interactions between this external magnetic field and the magnetic moments of the nuclei. The overall magnetization is characterized by a magnetic moment $\overrightarrow{M_0}$ which rotates around the direction of $\overrightarrow{B_0}$. This motion, called precession, occurs at a given frequency (called Larmor frequency) specific to each nucleus. NMR consists of perturbing this equilibrium state by applying a second magnetic field $\overrightarrow{B_1}$, perpendicular to $\overrightarrow{B_0}$ and pulsed during a short time. Due to electromagnetic radiation from $\overrightarrow{B_1}$, the overall magnetization temporarily changes from $\overrightarrow{M_0}$ to $\overrightarrow{M}$. When $\overrightarrow{B_1}$ is stopped, the system returns progressively to its equilibrium state ($\overrightarrow{M} \to \overrightarrow{M_0}$). This phenomenon is called relaxation. During NMR experiments, the time evolution of M is recorded and two characteristic times are determined. The first time (T_1) characterizes the relaxation time of the component of the vector $\overrightarrow{M}$ parallel to $\overrightarrow{B_0}$ (spin–lattice relaxation), while the second time (T_2) is the relaxation time of its components in the plane perpendicular to $\overrightarrow{B_0}$ (spin–spin relaxation).

In the case of porous materials, NMR experiments often concern the relaxation phenomenon of the proton ^{1}H. The characterization of pore structure is based on the existing dependence of the relaxation times, T_1 and T_2, on the pore size. In fact, the overall recorded relaxation time is the mean of the contribution of two terms: the relaxation of “bulk protons” (i.e. inside the porosity) and “surface protons” (i.e. at the pore surface).

For instance, Figure 1.6 gives relaxation rates ($1/T_1$) measured in the case of a cement paste, i.e. a material with a multiscale pores structure [KOR 07]. Four classes of relaxation rates can be observed, which reveals the dependency of the relaxation process on pore size. The two higher classes correspond to the smaller pore sizes (i.e. pores in Calcium-Silicate-Hydrate (CSH) gel), while the two lower classes can be associated with capillary pores.

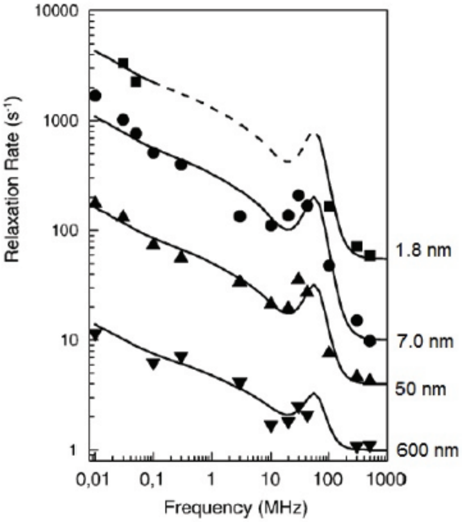

Figure 1.6. *Relaxation rates ($1/T_1$) versus Larmor frequency measured for a cement paste (cement = C_3S, W/C = 0.4, age =1 year). The four curves correspond to the material responses due to four average pore sizes (given on the right). The latter are calculated values by the authors [KOR 07]*

The use of NMR relaxometry for porous material characterization has some limits. Especially, the so-obtained relaxation times are usually given in milliseconds and cannot be easily converted in a size scale, for instance in nanometers. Such a conversion depends on experimental conditions and calculation methods [FAU 12]. Thus, results from relaxometry are mainly used to compare the evolution of relaxation times as a function of studied parameters. For instance, Figure 1.7 shows the time evolution of T_1 distribution measured for a cement paste at the early age. This evolution reveals the structuration of the material and the refining of the pore structure due to cement hydration. Another example is given in Figure 1.8, which shows the influence of cellulose ether on the time evolution of the relaxation rate ($1/T_1$) of cement pastes.

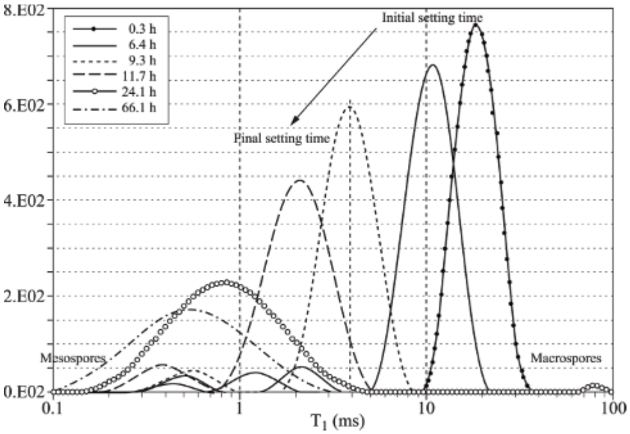

Figure 1.7. *Time evolution of the relaxation time T_1 distribution due to hydration of a cement paste at very early age (cement = OPC, W/C = 0.35) [WAN 13]*

In addition to the characterization of pore structure, NMR can also be used as an imaging technique (magnetic resonance imaging (MRI)). In this case, magnetic field gradients are applied in three directions (three-dimensional (3D) imaging). Consequently, the precession frequency of the protons immersed in the magnetic field depends on the location. This technique is used, for instance, to image water contents of porous materials [FAU 12]. Resolution of MRI (~1 mm) is, however, too low for this technique to be able to serve image pore structure.

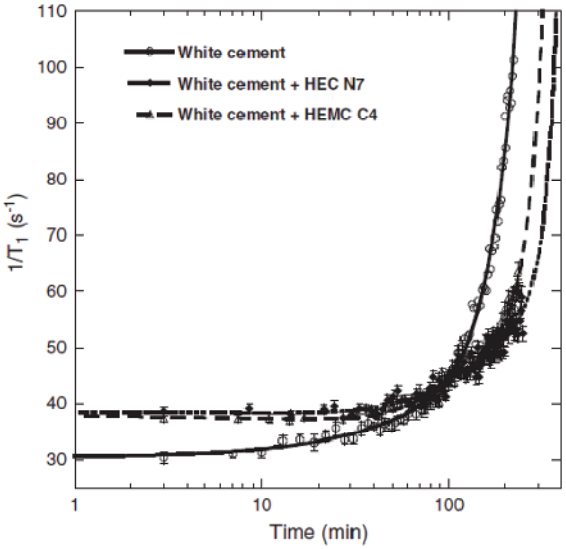

Figure 1.8. *Time evolution of the relaxation rate ($1/T_1$) measured at a Larmor frequency of 10 kHz for cement pastes (white cement, W/C = 0.4) – effect of the presence of two cellulose ether (HEC and HEMC) [PAT 12]*

1.2.4. *Imaging techniques*

Characterization methods shown previously, for instance MIP, give a first level of information on the pore structure, i.e. open porosity, pore size distribution or surface area. Of course, this is not enough to describe completely the voids network, since other characteristics, such as connectivity or pore shape, are not provided [SIN 04]. These characteristics are, however, very relevant for the modeling of transfer properties of materials with disordered pore structure, such as cementitious materials.

In this scope, imaging techniques are powerful tools [LEV 07]. Indeed, they permit a mapping of the pore structure in 3D which offers, among others, direct assessments of the connectivity.

Two families of imaging methods can be distinguished. The first family is based on the acquisition of 2D images of cut-sections of the material followed by a reconstruction of the pore structure in 3D. The second family consists of mapping the pore structure in 3D more directly, without any sample preparation such as slicing or polishing, e.g. computed X-ray microtomography or electron tomography.

1.2.4.1. *From 2D to 3D images of the pore structure*

Images in two dimensions can be obtained by many techniques. Scanning electron microscopy (SEM) and transmission electron microscopy (TEM) are undoubtedly the most popular techniques. In brief, SEM uses a focused beam of electrons, which interacts at the surface of solid specimens. In the case of TEM, the beam is transmitted through the specimen. The various signals generated by the electrons–specimen interactions give information about chemical composition and densities of the different phases in the material. For instance, from polished sections of cement-based materials, the detection of backscattered electrons (BSEs) in SEM facilitates the construction of high-resolution 2D images of the anhydrous and hydrated phases. In electron microscopy, the resolution can be less than the nanometer scale.

Before SEM imaging, the material porosity can also be injected by a metal, such as wood's metal or gallium [WIL 98, KUR 06]. The X-rays emitted by the specimen due to the electron beam can be observed using an electron probe microanalysis (EPMA). The so-measured repartition of the intruded metal provides a 2D map of the pore structure.

To obtain 3D images from 2D images, a serial cross-sectioning has to be performed. This consists of repeatedly polishing the observed specimen. After each polishing, a scanning of the obtained surface is performed by SEM, for instance. The reconstruction of the 3D image is done by stacking the 2D images, as shown in Figure 1.9.

In the polishing operation, the serial cross-sections should be as close as possible. Otherwise, the resolution of the 3D image reconstructed by stacking would not be the same in the direction perpendicular to polishing compared to the scanned section. To avoid this obvious shortcoming, the polishing operation can be performed directly in the SEM microscope by using a focus ion beam [MUN 09, LUR 11]. In a microscope equipped with Focused Ion Beam (FIB), a beam of ions such as gallium ions hits the specimen surface, resulting in an ablation of a few nanometers. Figure 1.10 gives a schematic representation of the FIB technique [KEL 11]. By coupling FIB and SEM, the serial sectioning and 3D reconstruction become much more accurate. Although this technique is promising, it has not been widely used for imaging the pore structure of cement-based materials. However, this latter is used more for applications regarding soil studies [HOL 10, NAD 13].

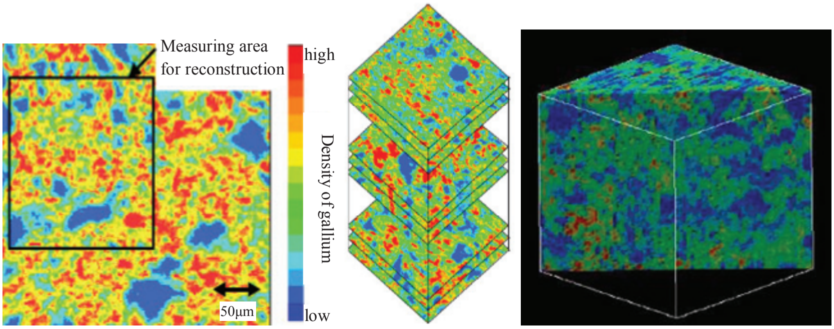

Figure 1.9. *3D reconstruction of the pore structure from 2D images stacking. The 2D images were obtained by EPMA on a cement paste sample intruded by gallium [KUR 06]. For a color version of the figure, see www.iste.co.uk/ait-mokhtar/coastal.zip*

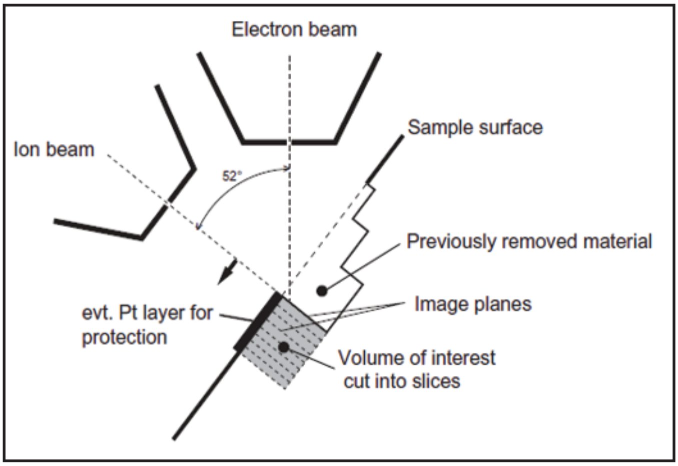

Figure 1.10. *Schematic representation of SEM coupled with FIB device [KEL 11]*

1.2.4.2. *Non-destructive 3D mapping by X-ray microtomography*

Computed X-ray microtomography (µCT) consists of subjecting a material sample to an X-ray source [LAN 10]. X-ray beam passing through the sample is more or less absorbed depending on the absorptivity of the various phases in the material. A plane detector is used to acquire a 2D image of the intensity spatial variations of the absorbed beam (projection image). The X-ray source is then rotated around the sample. A series of 2D projections are so-recorded. Based on the mathematical methods of inversion, such as Fourier transforms, it is possible to reconstruct a 3D image usually given with gray levels corresponding to the different absorption levels of the material phases. In the case of a porous material, since X-rays are mainly absorbed by the solid phase, µCT can provide a 3D map of the pore structure. When differences in absorption levels are less significant than in the case of solid/voids segmentation, image analysis methods, such as edge detection, can be necessary to extract spatial distribution of phases.

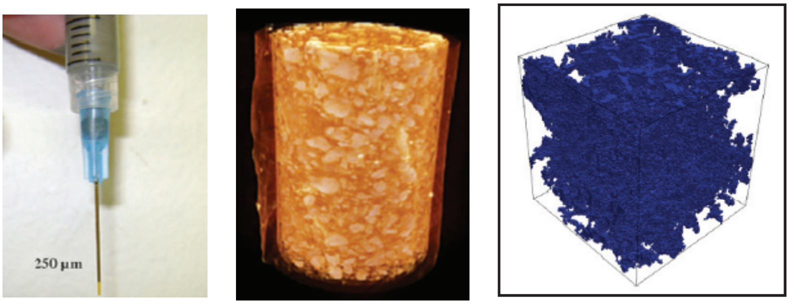

Figure 1.11. *Investigation of cement paste microstructure by X-ray microtomography. Sample of a plastic tube (left), reconstructed 3D image at 1 day age (middle), pore structure of a volume of interest (VOI) after image segmentation (right) [ZHA 12]. For a color version of the figure, see www.iste.co.uk/ait-mokhtar/coastal.zip*

X-ray microtomography is a completely non-destructive method. This is one of its main interests, as compared to 3D reconstruction based on 2D microscopy which needs polishing operations (see the previous section). One of the drawbacks of µCT can be its resolution which is currently of approximately 1 µm for a desktop apparatus, which is not enough to investigate the pore structure of materials such as cementitious materials. The latter contain many pores lower than 100 µm in diameter. For instance, µCT has been applied by Gallucci *et al.* for the study of the microstructure formation of cement paste between 1 and 60 days [GAL 07]. Beyond a few days, the resolution is not high enough to distinguish the pores of the cementitious matrix.

In the near future, µCT resolution is likely to be improved. Especially, in the case of synchrotron X-ray, resolution of lower than 500 µm per voxel is already obtained and porosity of cement-based materials can be investigated in more detail [PRO 09]. Investigations with high resolution are, however, limited to small-size specimens of cement pastes, as shown in Figure 1.11 [ZHA 12]. At lower resolution, µCT is an interesting tool increasingly used for the investigation of materials degradation phenomena, e.g. [LAN 00, ROU 09] (Figure 1.12).

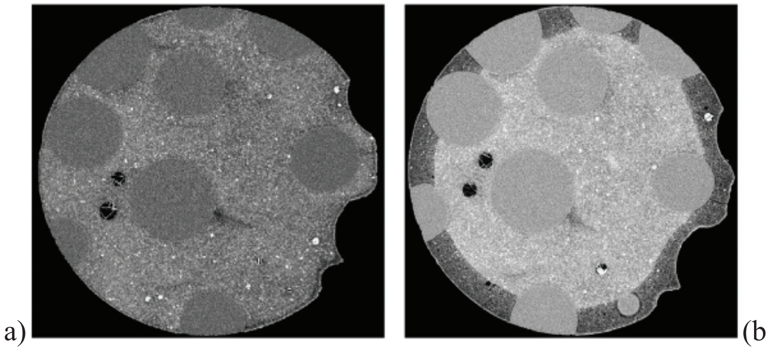

Figure 1.12. *A concrete leaching investigated by X-ray microtomography. Cross-section of a sound specimen before leaching a) and cross-section after 11 h of leaching b) [ROU 09]*

1.3. Some constructed models for porous microstructures

Experimental tests, such as MIP tests or moisture sorption/desorption tests, provide a pore size distribution using some assumptions dealing mainly with the geometrical shape of the pores within the material. From data provided by these techniques, the objective is to build models describing microstructures aiming linking them to mass transfer modeling for the prediction of degradation of structures, particularly in the case of chloride in coastal zones [AÏT 04].

1.3.1. *Models based on pore size distribution*

While providing results sometimes discussed [FAU 80, VAN 81, WAR 81, COO 93], MIP remains a powerful tool for characterizing the pore size distribution of a porous medium. However, let us recall that the physical properties of mercury as a liquid measurement are different from those of water, while water is the main, if not only, fluid carrying aggressive species within porous materials and dissolving certain fractions of hydrated compounds in the case of cementitious materials. Furthermore, mercury does not penetrate the smallest pores such as CSH[1] [HAL 95]. In addition, devices available actually limit the penetration to pores with 3 nm in diameter.

Despite these considerations, the technique is widely used for the characterization of porous media. Therefore, results provided by this technique are used for the construction of models describing the porous network properties.

1.3.1.1. *Statistical functions of pore size distribution*

In addition to the overall porosity ε_p, MIP test provides the logarithmic differential intrusion as a function of pore radius penetrated at a pressure *i* by unit volume of sample, which is nothing but the pore size distribution:

$$f(R_p) = -\frac{1}{L}\,\frac{V_{pi} - V_{p(i-1)}}{\ln R_{pi} - \ln R_{p(i-1)}} \qquad [1.6]$$

where R_{pi} and $R_{p(i-1)}$ are the radii penetrated, respectively, at stages *i* and $(i-1)$; V_{Pi} and $V_{p(i-1)}$ are the corresponding porous volumes and *L* is the samples length.

The plot of equation [1.6] can be modeled by a statistical distribution with a random variable, R_p, set by the results of MIP test.

The aim of the modeling that we propose is then a parametric characterization of the experimental pore size distribution for the calculation of other material properties such as specific area and permeability.

According to Diaz *et al.* [DIA 87], based on the assumption of cylindrical pores, some researchers have established simplified relationships between the pore volume and their entry diameters. Some other authors (e.g. [AÏT 99]) have presented models, called parallel channels, based on a

---

[1] Cement industry notations of the hydrated calcium silicates whose classical chemical formula is: $3CaO.2SiO_2.3H_2O$. We can also define them in a "generic" manner in the form $CaO.SiO_2.nH_2O$ [DUN 89].

probability calculation. This probabilistic aspect makes the use of these models difficult. As a first approach, we assume that the porous network is represented by cylindrical pores of different radii R_p with the same length L within the material with a unit representative surface (Figure 1.13).

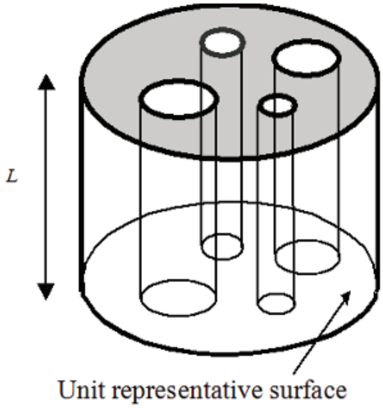

Figure 1.13. *Simplification of the porous structure referred to a unit representative surface*

Two main categories of pore size distribution may be found (Figure 1.14). First, we have the case where the distribution has only one "mode" pore radius around a single average, which is called "porosity peak". The pore structure is then a single porous mode, which is called a "single-mode structure". On the other hand, if the distribution has more than one group of radii around two or more "porosity peaks", the pore structure has then more porous modes and is qualified as "polymodal".

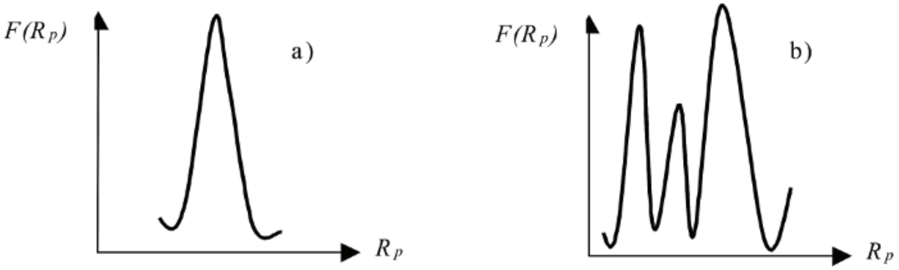

Figure 1.14. *Examples of pore size distributions: a) monomodal distribution and b) polymodal distribution*

1.3.1.1.1. Case of monomodal porous structures

We first discuss the case where the pore structure has only one mode, i.e. the distribution has a single "peak".

In this case and according to Shi *et al.* [SHI 89], we can express the number of pores per unit surface representative dn_p whose radii are between R_p and (R_p+dR_p) by a statistical distribution of log-normal type, but use here the total number of pores per unit surface representative n_p:

$$dn_p = \frac{n_p}{\xi\sqrt{2\pi}}\exp\left(-\frac{\ln^2(R_p/R_{pm})}{2\xi^2}\right)d(\ln R_P) \tag{1.7}$$

where ξ is a location parameter which is dimensionless and ensures that dn_p is the probability density function for the area [0; ∞[, R_{pm} is the statistical average pore radius and n_p is the number of pores per unit surface.

To the variation dn_p corresponds the following elementary variation of volume between R_p and (R_p+dR_p):

$$dV_p = \pi R_p^2 L dn_p \tag{1.8}$$

From equations [1.6]–[1.8], we obtain:

$$f(R_p) = \frac{\pi R_p^2 n_p}{\xi\sqrt{2\pi}}\exp\left(-\frac{\ln^2(R_p/R_{pm})}{2\xi^2}\right) \tag{1.9}$$

which allows a maximum α such that:

$$\left\{\begin{array}{l} R_{p\max} = R_{pm}e^{2\xi^2} \\ \alpha = f(R_{p\max}) = \dfrac{\pi R_{pm}^2 n_p}{\xi\sqrt{2\pi}}e^{2\xi^2} \end{array}\right\} \tag{1.10}$$

The porosity per surface unit is obtained from [1.1], [1.7] and [1.8]:

$$\varepsilon_p = \frac{1}{\sqrt{2\pi}} \int_0^\infty \frac{\pi R_p^2 n_p}{\xi} \exp\left(-\frac{\ln^2 (R_p / R_{pm})}{2\xi^2} \right) d(\ln R_p) \tag{1.11}$$

whose solution is:

$$\varepsilon_p = \pi R_{pm}^2 n_p e^{2\xi^2} \tag{1.12}$$

From [1.10] and [1.12], we obtain:

$$\begin{aligned} \xi &= \frac{\varepsilon_p}{\alpha\sqrt{2\pi}} \\ R_{pm} &= \frac{R_{p\max}}{e^{2\xi^2}} \\ n_p &= \frac{\varepsilon_P}{\pi R_{Pm}^2 e^{2\xi^2}} \end{aligned} \tag{1.13}$$

The MIP test provides the porosity ε_p and the pore size distribution of the material. From the latter, R_{pmax} and α are obtained. Using these two experimental data, parameters [1.13] are calculated. Thus, we obtain the probability law of pore size distribution (equation [1.9]). This law can be used for the determination of other transport properties of the medium and for the upscaling in behavior modeling of heterogeneous media [AMI 01a, AMI 01b].

1.3.1.1.2. Case of polymodal porous structures

In the event that there is N porous mode, i.e. N peaks, the pore size distribution is divided up into N elementary classes according to the number of peaks. Then, the expression of the pore number will be the sum of elementary functions of distribution with the same random variable R_p:

$$dn_p = \frac{1}{\sqrt{2\pi}} \sum_{j=1}^{N} \frac{n_{pj}}{\xi_j} \exp\left(-\frac{\ln^2 (R_p / R_{pmj})}{2\xi_j^2} \right) d(\ln R_P) \tag{1.14}$$

With each porous mode is associated an elementary porosity ε_{pj} and an elementary pore size distribution law with the following parameters:

$$\xi_j = \frac{\varepsilon_{pj}}{\alpha_j\sqrt{2\pi}}$$

$$R_{pmj} = \frac{R_{p\max j}}{e^{2\xi_j^2}} \qquad [1.15]$$

$$n_{pj} = \frac{\varepsilon_{pj}}{\pi R_{pmj}^2 e^{2\xi_j^2}}$$

1.3.1.1.3. Determination of the pore-specific area

Based on the assumption that the pore-specific area is only linked to the arithmetic average of pore radii penetrated by the mercury during the test, MIP acquisition devices generally provide a value of this parameter. To ensure consistency in the use of MIP results, a relationship can be built by integrating the statistical pore size distribution.

Given the assumption of cylindrical pores, to the elementary pore volume dV_p (equation [1.8]) corresponds an elementary surface dA_p developed by pores having radii between R_p and $(R_p + dR_p)$, whose expression is:

$$dA_p = 2\pi R_p L dn_p \qquad [1.16]$$

Reduced to a unit volume of material, the elementary-specific area is obtained:

$$da_p = 2\pi R_p dn_p \qquad [1.17]$$

The pore surface area of the material can be obtained by the integration of equation [1.17], in which d_{np} is substituted by its expression (equation [1.7]):

$$a_p = 2\pi R_{pm} n_p e^{\frac{1}{2}\xi^2} \qquad [1.18]$$

1.3.1.2. *Models including geometrical parameters*

The approach described above is based on the main assumption that the pores are cylindrical, i.e. neither tortuosity nor constrictivity is considered. It means that construction materials are known to have microstructures with complex geometries, where parameters such as tortuosity, constrictivity or connectivity of the pores play a significant role in the transfer of aggressive agents, and then in the structures durability. Hereafter, an approach describing these parameters is presented.

Based on the isotropic porous network model in a cubic representative elementary volume (REV) proposed by Aït-Mokhtar *et al.* [AÏT 02], let us consider a wider scheme (Figure 1.15), with pores having different lengths $l_1, l_2, ..., l_n$ and different sections $S_1, S_2, ..., S_n$. These sections are classified such as $S_1 > S_2 > ... > S_n$ (Figure 1.16). Then, we can define the tortuosity as [AMI 05]:

$$\tau = \left(\frac{l_1 + l_2 + ... + l_n}{l} \right) = \left(\frac{1}{l} \sum_{i=1}^{n} l_i \right) \qquad [1.19]$$

The contraction effect and the pores length ratio are introduced, respectively, by m_{ij} and q_{ij}:

$$m_{ij} = \frac{S_j}{S_i};\ q_{ij} = \frac{l_j}{l_i} \qquad [1.20]$$

where $S_i > S_j$ if $i < j$.

Then, tortuosity becomes:

$$\tau = \frac{l_n}{l} \sum_{i=1}^{n} \frac{1}{q_{in}} \qquad [1.21]$$

Given the configuration of Figures 1.15 and 1.16, N^3 is the number of elementary cubes per representative sample of material with cubic shape. Then, the total pore section S_p and the total section S of the material cube are, respectively:

$$S_p = \frac{(n!+1)^2}{n} N^2 \sum_{i=1}^{n} S_i \text{ and } S = (n!+1)^2\, l^2 N^2 \qquad [1.22]$$

Given the pore entry section on an elementary cube surface, the porous volume and the global volume of the representative material are, respectively:

$$V_P = 3\left(n!+1\right)^3 N^3 \sum_{i=1}^{n} S_i l_i \text{ and } V = (n!+1)^3 l^3 N^3 \qquad [1.23]$$

We deduce from [1.25], [1.22] and [1.23] the porosity of the material:

$$\varepsilon_P = \frac{V_P}{V} = \frac{3\left(n!+1\right)^3 N^3 \sum_{i=1}^{n} S_i l_i}{(n!+1)^3 l^3 N^3} = \frac{3}{l^3}\sum_{i=1}^{n} S_i l_i = 3\tau \frac{S_n}{l^2} \frac{\sum_{i=1}^{n} \frac{1}{m_{in} q_{in}}}{\sum_{i=1}^{n} \frac{1}{q_{in}}} \qquad [1.24]$$

where:

$$l = \sqrt[3]{\frac{3}{\varepsilon_p}\sum_{i=1}^{n} S_i l_i} \text{ and } \tau = \left(\frac{\varepsilon_p}{3\pi \sum_{i=1}^{n} R_i^2 l_i}\right)^{1/3} \left(\sum_{i=1}^{n} l_i\right) \qquad [1.25]$$

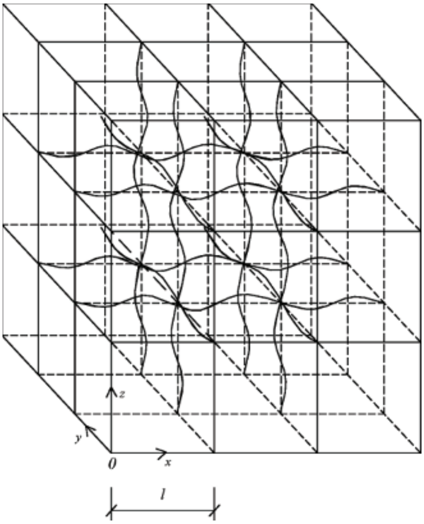

Figure 1.15. *Schematic view of the porous network in a cubic representative elementary volume (REV)*

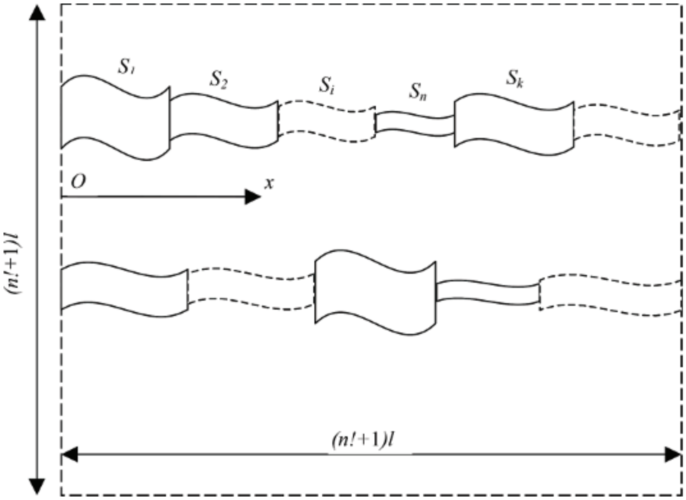

Figure 1.16. *A cross-section of the material*

A more recent work presented by Khaddour *et al.* [KHA 13, KHA 15] gives a simplified method for microstructure representation based on MIP data. This microstructure consists of parallel, cylindrical and tortuous pores of different diameters crossing the sample as shown in Figure 1.17. The total length of a pore of diameter d_i and volume V_{pi} is calculated using equation [1.26]:

$$L_i = \frac{4V_{pi}}{\pi d_i^2} \qquad [1.26]$$

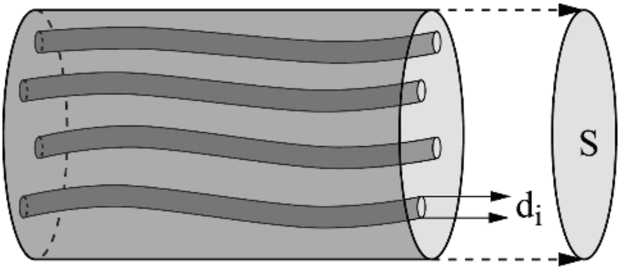

Figure 1.17. *Microstructure obtained from parallel pores assembly [KHA 15]*

A pore crosses the porous media sample if its length L_i reaches a critical length L_c (equation [1.27]) which depends on the sample thickness L_e and the pores tortuosity τ:

$$L_c = \tau \cdot L_e \qquad [1.27]$$

$$L_e = \sqrt[3]{V_t} \qquad [1.28]$$

where V_t is the total volume of the porous media containing x_i pores of diameter d_i. The quantity x_i is the characteristic quantity of the pore size distribution.

A pore that does not cross the sample, i.e. one whose length L_i does not reach the value of the critical length L_c, is connected to the pore with the next smallest diameter in order to obtain a serial assembly of pores with decreasing diameters as shown in Figure 1.18 [KHA 09].

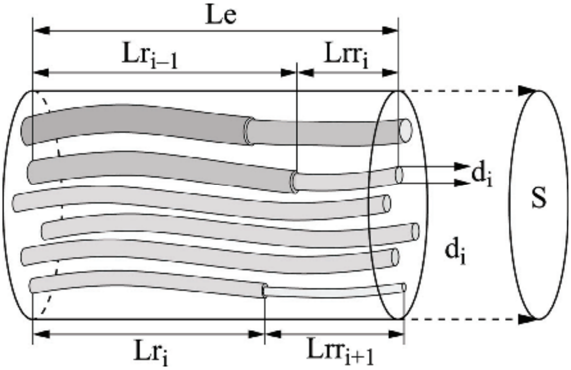

Figure 1.18. *Microstructure obtained from parallel and serial pores assembly [KHA 09]*

According to Figure 1.18, the total length of the pores of a diameter d_i is given by equation [1.29] as follows:

$$L_i = Lrr_i + x_i L_c + Lr_i \qquad [1.29]$$

1.3.2. *Tridimensional-constructed microstructures*

Microstructures of porous materials can be modeled from input data, such as pore size distribution, provided by various experimental techniques. Another approach consists of modeling the different phenomena involved in the formation of the pore structure. Such approaches were developed especially in the field of cementitious materials. Hydration of Portland cement has extensively been studied during the last century (and is still ongoing), resulting in accurate models of hydration kinetics. From such models, the formation of the microstructure of a cement paste can be computed from stacks of anhydrous cement grains whose volume progressively increases due to the hydration. This facilitates obtaining pore structures in 3D and information on percolation of the pore network. Of course, the realism of the computed microstructure greatly depends on the initial stacks of cement (grains shape, size distribution) and on the hydration model [SCR 04].

In the following, some approaches are described for the construction of evolving microstructures of cementitious materials. For most of the models described, the materials do not exceed the scale of cement pastes. For this microstructure construction, two kinds of approaches are commonly used: vectorial expansion approach of the cement grains and a 3D voxel-segmented image approach. Finally, an ideal way for the cement paste microstructure construction is presented on the basis of regular spherical grains stacks.

1.3.2.1. *Vectorial approach*

The first approach is based on a vector expansion of the anhydrous cement grains composing the stack. Two examples are given here:

– The first example, named hydration, morphology and structural development (HYMOSTRUC), was developed by van Breugel [VAN 91, VAN 95] and based on the work of Berlage [BER 87]. This model considers all the chemical phases of the cement and assumes that the cement grains are spherical. The hydration products are formed around these grains in dissolution. The density of reaction products is supposed to be constant during the hydration. The development of the microstructure depends on the interaction between the particles of different sizes. Thus, it is important that such a model considers the particle size distribution of cement grains as well as their spatial distribution.

A schematic view of the particle hydration is given in Figure 1.19.

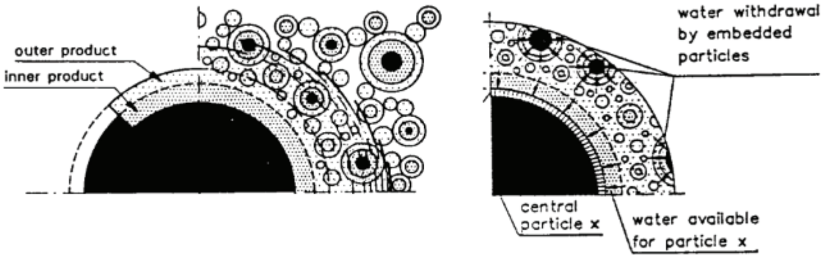

Figure 1.19. *Schematic representation of expansion mechanism during cement hydration [VAN 95]*

– The second example, called "µic" model, was developed by Bishnoi and Scrivener [BIS 09] to succeed the "IPKM" model developed by Pignat and Navi [PIG 05]. The "µic" model is based on the same approach like theHYMOSTRUC. The main difference lies in the segmentation of the volume into smaller cubes to make the calculation of the interaction between particles faster. In addition, the "µic" model facilitates the simulation of cement hydration in the presence of other materials such as fillers and mineral additives. The proportion of various materials is defined by volumes calculated using the stoichiometry of the reactions and the density of each individual phase.

At the output of these two models, we can obtain a 3D microstructure shown in Figure 1.20.

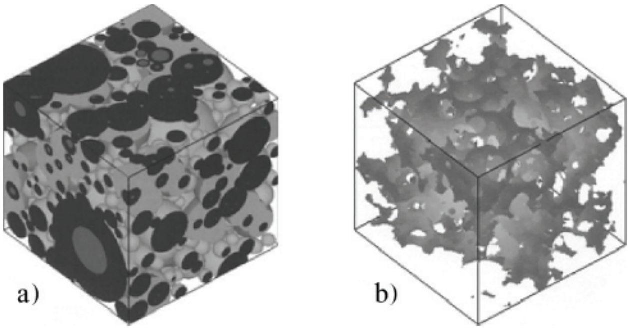

Figure 1.20. *3D representation of the microstructure obtained: a) solid phase and b) pore network [PIG 05]*

1.3.2.2. *Voxel-based method*

A second approach for microstructure construction is based on randomly stacked cement grains in a cubic volume. For this method, the model named CEMHYD3D, which was developed by Bentz at the NIST[2] in 1997 [BEN 97], is the most efficient model. This model was improved by Bullard [BUL 14] and is now named as VCCTL.

Such a model makes the simulation of the cement hydration possible, the use of mineral additions and aggregates and the microstructure development of a 3D stacking of cement grains. The considered cement grains may be spherical or may take a realistic shape of cement particles. Typically, the built 3D microstructure consists of a cube of sides 200 µm composed of 200 × 200 × 200 microcubes of side 1 µm. These microcubes (voxels) are the smallest and indivisible element of the microstructure and contain only one chemical phase of the cement.

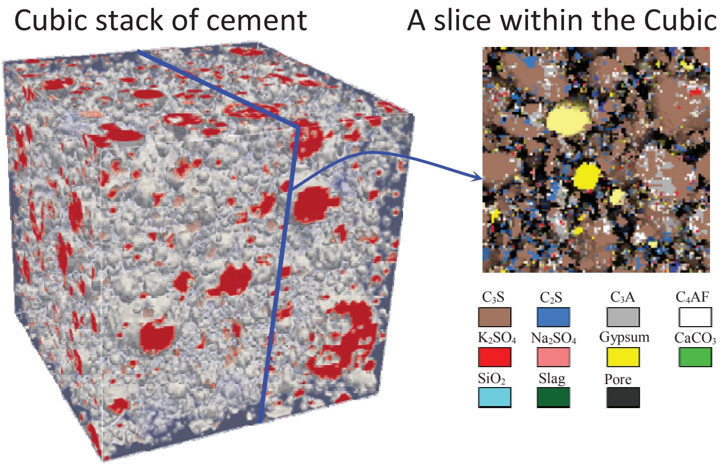

Figure 1.21. *Schematic representation of the obtained anhydrous microstructure. For a color version of the figure, see www.iste.co.uk/ait-mokhtar/coastal.zip*

The input data of this model correspond to the real properties of the considered materials. Cement hydration is performed through several cycles of dissolution–precipitation–chemical reaction. The hydration products are formed in the space between the cement grains and around the latter in

---

[2] National Institute of Standard and Technology, USA.

dissolution. The output data are the porosity, the degree of hydration, the fractions of percolated porosity and solid, the heat released by the reaction, the fractions of hydration products, the chemical shrinkage and several other properties [BUL 14]. Figures 1.21 and 1.22 give a schematic view of the microstructure before and after hydration.

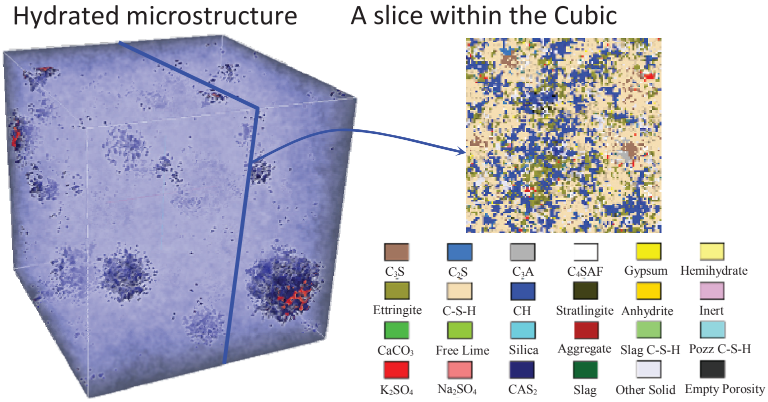

Figure 1.22. *Schematic representation of the hydrated microstructure. For a color version of the figure, see www.iste.co.uk/ait-mokhtar/coastal.zip*

1.4. Some approaches for linking microstructure data to permeability

Transfer of aggressive agents is closely related to the permeability of the porous medium, since these transfers are made possible by water during its circulation in the medium. Predicting the permeability as a function of the microstructure data is then important. In the following, after a brief definition of the permeability, some models of permeability based on the investigation or modeling of microstructures of materials are presented.

The permeability of a porous medium represents its ability to be crossed by a fluid under a total pressure gradient. This permeability can be obtained by using Darcy's law for laminar flow of a Newtonian fluid. This law, given by equation [1.30], expresses the relationship between the flow velocity v and the total pressure gradient ∇P. This relationship also depends on the dynamic viscosity η and the permeability K:

$$v = -\frac{K}{\eta}\nabla P \qquad [1.30]$$

The permeability K can only be assessed based on intrinsic parameters such as porosity ε_p and the critical pore diameter D_c as shown in Figure 1.23 [HAM 12]. The critical diameter D_c corresponds to the smallest section pore crossed by the fluid.

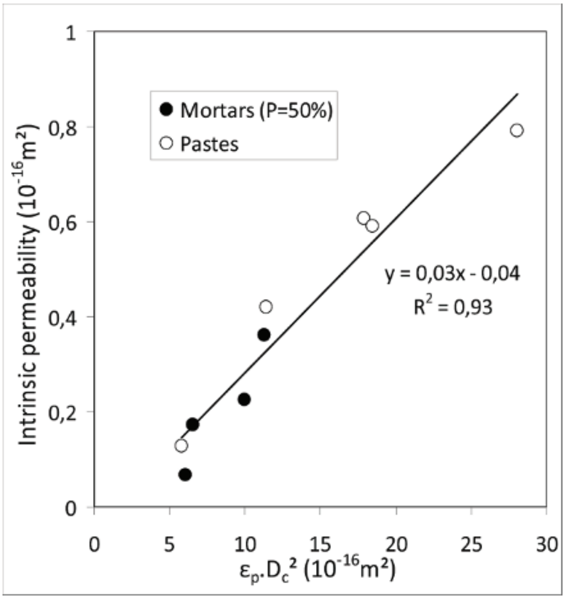

Figure 1.23. *Correlation between the intrinsic gas permeability of cementitious materials (pastes and mortars made with various water to cement ratios) and the pore structure parameter* $\varepsilon_p.D_c^2$ *[HAM 12]*

1.4.1. *Permeability from MIP tests*

1.4.1.1. *Case of cylindrical pores*

The approach described above is based on the assumption that the pores are cylindrical, i.e. neither tortuosity nor constrictivity is considered. It means that construction materials are known to have microstructures with complex geometries, where parameters such as tortuosity, constrictivity or connectivity of the pores play a significant role in the transfer of aggressive agents, and then in the structures durability. In the following, an approach describing these parameters is presented.

In the case of a viscous and laminar flow, the permeability of a porous medium K is expressed according to Darcy and Hagen's law as follows:

$$K = \frac{\varepsilon_p}{8} \frac{\sum_{1}^{\infty} V_{pi} R_{pi}^2}{\sum_{1}^{\infty} V_{pi}} \qquad [1.31]$$

Many works have been conducted on the relationship between permeability and pore structure. Researchers such as Holly *et al.* [HOL 93] based their approach on other works [AIT 57, SHI 89] to build numerical relationship in order to link these two parameters. Other researchers [BRO 92, OLL 92, REI 92] have solved equation [1.31] with the assumption of equal pore radii, i.e. with neglecting the random variable R_p and the statistical distribution. Then an analytical relationship of permeability is suggested according to some microstructure parameters.

Taking into account equations [1.7] and [1.8], resolution of [1.31] leads to:

$$K = \frac{\varepsilon_p}{8} R_{pm}^2 e^{6\xi^2} \qquad [1.32]$$

If the microstructure is polymodal with a pore size distribution with N peaks, the expression of the permeability becomes:

$$K = \sum_{j=1}^{N} \frac{\varepsilon_{pj}}{8} R_{pmj}^2 e^{6\xi_j^2} \qquad [1.33]$$

1.4.1.2. *Case of more complex geometrical shape of pores*

Let us consider a laminar and unidirectional fluid flow, with dynamic viscosity μ, along the Ox axis in the porous medium of Figure 1.15 and dP_i be the pressure difference between the entry and the exit of each pore with section S_i. Given the Poiseuille law, the volumic flow rate dq_i of fluid in capillary with radius R_i and length l_i is:

$$dq_i = -\frac{\pi R_i^4}{8\mu} \frac{dP_i}{l_i} = -\frac{S_i^2}{l_i} \frac{dP_i}{8\mu\pi} \qquad [1.34]$$

The flow conservation in successive pores with sections S_i and S_j leads to $dq_i = dq_j = dq$. The global volumic flow rate Q through the pore structure is:

$$Q = \frac{(n!+1)^2}{n} N^2 \sum_{i=1}^{n} dq_i = (n!+1)^2 N^2 dq \qquad [1.35]$$

and the total pressure difference along the length l is $dP = \sum_{i=1}^{n} dP_i$. Given equations [1.34] and [1.35], we obtain:

$$dP = dP_n \sum_{i=1}^{n} \left(\frac{m_{in}^2}{q_{in}} \right) \qquad [1.36]$$

We note that ΔP is the total pressure difference between the parallel sides of the cubic porous medium with distance L ($L = 1$ is the unit porous medium thickness) such that:

$$\Delta P = (n! + 1)NdP \text{ and } L = (n! + 1)lN \qquad [1.37]$$

Given the average flow velocity $u = Q/S$ and according to Darcy's law $K = -\frac{\mu L}{\Delta P} u$, the combination of equations [1.21], [1.22], [1.24], [1.35] and [1.36] leads to the intrinsic permeability:

$$K = \frac{\delta \varepsilon_p}{24 \tau^2} R_n^2 \qquad [1.38]$$

where δ is the constrictivity factor such that:

$$\delta = \frac{\left(\sum_{i=1}^{n} \frac{1}{q_{in}} \right)^2}{\left(\sum_{i=1}^{n} \frac{1}{q_{in} m_{in}} \right) \left(\sum_{i=1}^{n} \frac{m_{in}^2}{q_{in}} \right)} \qquad [1.39]$$

The permeability of a multimodal material represented by the serial/parallel pores assembly proposed by Khaddour *et al.* [KHA 13, KHA 09] (see section 1.3.2.1.2) is estimated by a combination of

Poiseuille's law (at the microscale) and Darcy's law (at the macroscale). At the microscale, the volume flow Q through the pore of a diameter d_i generated by a pressure gradient at the sample borders ($\Delta P = P_1 - P_2$) is decomposed into: (i) the flow Q_p through the pores in parallel (equation [1.40]) and (ii) the flow Q_a through the pores in series (equation [1.41]):

$$Q^p = \sum_{i=1}^{N} x_i Q_i^p = \frac{\pi}{256\mu} \frac{P_1^2 - P_2^2}{L_c P_2} \sum_{i=1}^{N} x_i d_i^4 \quad [1.40]$$

$$Q^a = \sum_{i=1}^{N} Q_i^a = \frac{\pi}{256\mu} \frac{P_1^2 - P_2^2}{P_2} \sum_{i=1}^{N} \frac{1}{\left(\sum_{k=i}^{j-1} \frac{Lr_k}{d_k^4}\right) + \frac{Lrr_j}{d_j^4}} \quad [1.41]$$

$$Q = Q^p + Q^a = \frac{\pi}{256\mu} \sum_{i=1}^{N} \left(\frac{x_i d_i^4}{L_c} + \frac{1}{\left(\sum_{k=i}^{j-1} \frac{Lr_k}{d_k^4}\right) + \frac{Lrr_j}{d_j^4}} \right) \quad [1.42]$$

Figure 1.24 gives a schematic representation of a serial assembly with the parameters needed for Q^a calculation.

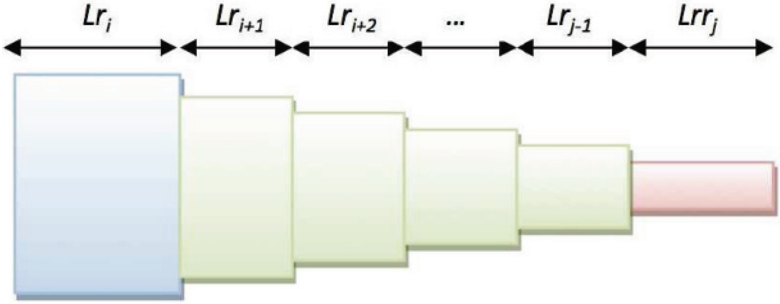

Figure 1.24. *Serial pores assembly from diameter d_i to d_j [KHA 13]. For a color version of the figure, see www.iste.co.uk/ait-mokhtar/coastal.zip*

The permeability is obtained at the macroscale by using the Darcy’s law, without considering the sliding effect at the pore wall, following equation [1.43]:

$$K = \frac{\pi L_c}{128 S\tau} \sum_{i=1}^{N} \left(\frac{x_i d_i^4}{L_c} + \frac{1}{\left(\sum_{k=i}^{j-1} \frac{Lr_k}{d_k^4} \right) + \frac{Lrr_j}{d_j^4}} \right) \qquad [1.43]$$

1.4.2. *Permeability from constructed microstructures*

1.4.2.1. *Permeability determination from network of capillaries*

From 3D representations of the pore structure, obtained by imaging techniques (see section 1.2.4) or by modeling (see section 1.3.2), permeability can be calculated from a network of capillaries which is placed inside the porosity [PIG 05, BIS 09, YE 06]. From this simplification of the pore structure, it is relatively easy to calculate the permeability of the network using Hagen–Poiseuille law (as shown in the previous section). In order to illustrate this approach, let us consider the determination of the permeability made by Ye *et al.* for their simulated microstructure of cement paste as shown in Figure 1.25 [YE 06].

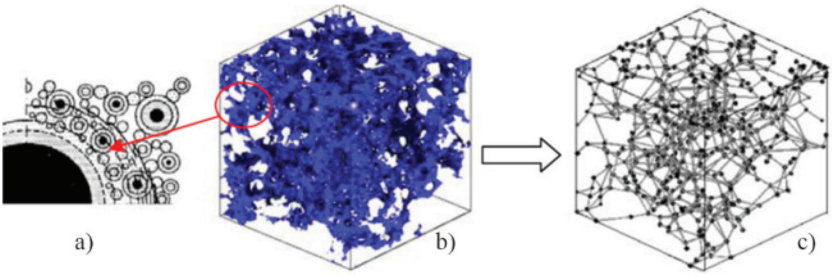

Figure 1.25. *Porous network obtained microstructure from HYMOSTRUC model: a) at the scale of grains, b) real obtained microstructure and c) simulated microstructure by connected cylindrical tubes [YE 06]. For a color version of the figure, see www.iste.co.uk/ait-mokhtar/coastal.zip*

The hydraulic conductivity g_{ij} (equation [1.44]) is calculated for each capillary and placed between peaks i and j of the network:

$$g_{ij} = \frac{\pi R_{\min}^4}{64 \Delta d} \qquad [1.44]$$

where Δd is the distance between peaks i and j, and R_{min} is the minimum hydraulic radius of the branch, i.e. the minimum of R_i at peak i and R_j at peak j.

The flux q_{ij} in each capillary is then calculated according to Hagen–Poiseuille law following equation [1.45]:

$$q_{ij} = g_{ij} \frac{\Delta P_{ij}}{\eta} \qquad [1.45]$$

where ΔP_{ij} is the pressure difference between peaks i and j, and η is the dynamic viscosity of the fluid crossing the microstructure.

The intrinsic permeability K of the obtained microstructure is directly calculated by Darcy's law following equation [1.46] [YE 06] by requiring a pressure difference ΔP across the pore network (Figure 1.26):

$$K = \frac{LQ}{A \Delta P} \eta \qquad [1.46]$$

where Q is the average total flux at the outlet of the microstructure sample, A is the cross-sectional area of the sample and L is the length of the sample in the direction of the flow.

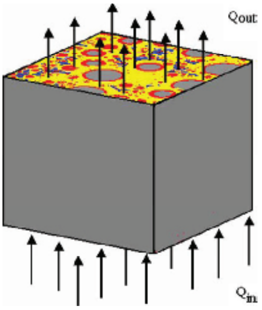

Figure 1.26. *One-dimensional flow representation through the simulated microstructure [YE 06]. For a color version of the figure, see www.iste.co.uk/ait-mokhtar/coastal.zip*

1.4.2.2. *Permeability determination by Stokes equation resolution*

Another approach consists of solving the equation modeling transfer by permeation, for instance the Stokes equation [1.47], directly in the constructed or measured 3D pore structure. This can be done by meshing the porosity, and using computation method such as FEM or the finite volume method.

For instance, this method was proposed by Bentz for the microstructure of cement paste computed by CEMHYD3D [BEN 07].

$$\begin{cases} \mu\nabla^2 v = \nabla p \\ \nabla \cdot v = 0 \\ v = 0 \quad \text{at solid/fluid interface} \end{cases} \qquad [1.47]$$

The resolution of Stokes equations needs the pressure gradient as input data and gives an average outlet velocity of the fluid flow. The permeability is then calculated from this velocity according to Darcy's law, as done in [1.46].

1.5. Bibliography

[AFN 10] AFNOR, Standard NF P18-459: Béton – Essais pour béton durci – Essai de porosité et de masse volumique, 2010.

[AFP 97] AFPC-AFREM (Association Française de Recherches et Essais sur les Matériaux) (sous la direction de Ollivier J.P.), Durabilité des bétons: Méthodes recommandées pour la mesure des grandeurs associées à la durabilité, Comptes rendus des Journées Techniques, Toulouse, France, 11–12 December 1997.

[AIT 57] AITCHISON J., BROWN J.A.C., *The Log-Normal Distribution*, Chapter 10, Cambridge University Press, 1957.

[AÏT 99] AÏT-MOKHTAR A., AMIRI O., SAMMARTINO S., "Analytic modeling and experimental study of the porosity and the permeability of porous media, application to cement mortars and granitic rocks", *Magazine of Concrete Research*, vol. 51, no. 6, pp. 391–396, 1999.

[AÏT 02] AÏT-MOKHTAR A., AMIRI O., DUMARGUE P. *et al.*, "A new model to calculate water permeability of cement based materials from MIP results", *Advances in Cement Research*, vol. 14, no. 2, pp. 43–49, 2002.

[AÏT 04] AÏT-MOKHTAR A., AMIRI O., POUPARD O. *et al.*, "A new method for determination of chloride flux in cement-based materials from chronoamperometry", *Cement and Concrete Composites*, vol. 26, pp. 339–345, 2004.

[AMI 01a] AMIRI O., AÏT-MOKHTAR A., DUMARGUE P. *et al.*, "Electrochemical modeling of chlorides migration in cement-based materials, Part 1. Theoretical basis at microscopic scale", *Electrochimica Acta*, vol. 46, pp. 1267–1275, 2001.

[AMI 01b] AMIRI O., AÏT-MOKHTAR A., DUMARGUE P. *et al.*, "Electrochemical modeling of chlorides migration in cement-based materials, Part 2. Experimental study – calculation of chlorides flux", *Electrochimica Acta*, vol. 46, pp. 3589–3597, 2001.

[AMI 05] AMIRI O., AÏT-MOKHTAR A., SARHANI M., "Three-dimensional modeling of cementitious materials permeability from polymodal pore-size distribution obtained by MIP tests", *Advances in Cement Research*, vol. 17, pp. 39–45, 2005.

[ARL 07] ARLIGUIE G., HORNAIN H., *GranDuBé: Grandeurs associées à la durabilité des bétons*, Presses de l'Ecole Nationale des Ponts et Chaussées, 2007.

[BAR 51] BARRETT P., JOYNER G., HALEND P., "The determination of pore volume and area distributions in porous substances. Computations from nitrogen isotherms", *American Chemical Society*, vol. 73, pp. 373–380, 1951.

[BAR 98] BAROGHEL-BOUNY V., "Texture and moisture properties of ordinary and high-performance cementitious materials", *Proceedings of the International Rilem Conference*, *Concrete from Material to Structure*, Arles, 1998.

[BEN 97] BENTZD P., "Three-dimensional computer simulation of Portland cement hydration and microstructure development", *Journal of the American Ceramic Society*, vol. 80, no. 1, pp. 3–21, 1997.

[BEN 07] BENTZ D.P., MARTYS N.S., A Stokes permeability solver for three-dimensional porous media, NIST internal Report 7416, 2007.

[BER 87] BERLAGE A.J.C., Strength development of hardening concrete, PhD Thesis, Delft University of Technology, Delft, The Netherlands, 1987.

[BIS 09] BISHNOI S., SCRIVENER K.L., "μic: a new platform for modeling the hydration of cements", *Cement and Concrete Research*, vol. 39, no. 4, pp. 266–274, 2009.

[BRO 92] BROWN P.W., SHI D., SKALNY J.P., "Porosity – permeability relationships", in SKALNY J. (ed.), *Materials Science of Concrete*, American Ceramic Society, pp. 83–109, 1992.

[BRU 38] BRUNAUER S., EMMETT P.H., TELLE E., “Adsorption of gases in multimolecular layers”, *American Chemical Society*, vol. 60, no. 2, pp. 309–319, 1938.

[BUL 14] BULLARD J.W., *Virtual Cement and Concrete Testing Laboratory. Version 9.5 User Guide*, NIST Special Publication 1173, 2014.

[CHO 06] CHOINSKA M., Effet de la température, du chargement mécanique et de leurs interactions sur la perméabilité du béton de structure, PhD Thesis, Central School of Nantes – University of Nantes, France, 2006.

[COO 93] COOK R.A., HOVER K.C., “Mercury porosimetry of cement-based materials and associated correction factors”, *ACI Materials Journal*, vol. 90, pp. 152–161, 1993.

[DIA 87] DIAZ C.E., CHATZIS I., DULLIEN F.A.L., “Simulation of capillary pressure curves using Bond correlated site percolation on a cubic network”, *Transport in Porous Media*, vol. 2, pp. 215–240, 1987.

[DIA 00] DIAMOND S., “Mercury porosimetry: an inappropriate method for the measurement of pore size distribution in cementitious materials”, *Cement and Concrete Research*, vol. 30, no. 10, pp. 1517–1525, 2000.

[DUN 89] DUNSTER A.M., “An interpretation of the carbonation of the cement paste using trimethysilation”, *Advances in Cement Research*, vol. 2, pp. 99–106, 1989.

[FAU 80] FAUDOT D., “Etude structurale d’un corps poreux”, *Pétrole et techniques*, vol. 273, pp. 19–29, 1980.

[FAU 12] FAURE P.F., CARÉ S., MAGAT J. *et al.*, “Drying effect on cement paste porosity at early age observed by NMR methods”, *Construction and Building Materials*, vol. 29, pp. 496–503, 2012.

[GAL 07] GALLUCCI E., SCRIVENER K.L., GROSO A. *et al.*, “3D experimental investigation of the microstructure of cement pastes using synchrotron X-ray microtomography (μCT)”, *Cement and Concrete Research*, vol. 37, no. 3, pp. 360–368, 2007.

[HAL 95] HALAMICKOVA P., DETWILER R.J., BENTZ D.P., *et al.*, “Water permeability and chloride ion diffusion in Portland cement mortars: relationship to sand content and critical pore diameter”, *Cement and Concrete Research*, vol. 25, pp. 790–802, 1995.

[HAM 09] HAMAMI A.A., Vers une prédiction de la perméabilité au gaz à partir de la composition des matériaux cimentaires, PhD Thesis, University of La Rochelle, 2009.

[HAM 12] HAMAMI A.A., TURCRY P., AÏT-MOKHTAR A., "Influence of mix proportions on microstructure and gas permeability of cementpastes and mortars", *Cement and Concrete Research*, vol. 42, no. 2, pp. 490–498, 2012.

[HOL 93] HOLLY J., HAMPTON D., THOMAS A., "Modeling relationships between permeability and cement paste pore microstructures", *Cement and Concrete Research*, vol. 23, pp. 1317–1330, 1993.

[HOL 10] HOLZER L., MÜNCH B., RIZZI M. *et al.*, "3D-microstructure analysis of hydrated bentonite with cryo-stabilized pore water", *Applied Clay Science*, vol. 47, nos. 3–4, pp. 330–342, 2010.

[KEL 11] KELLER L.M., HOLZER L., WEPF R. *et al.*, "On the application of focused ion beam nanotomography in characterizing the 3D pore space geometry of Opalinus clay", *Physics and Chemistry of the Earth*, vol. 36, no. 17–18, pp. 1539–1544, 2011.

[KHA 09] KHADDOUR F., Amélioration de la production de gaz des Tight Gas Reservoirs , PhD Thesis, University of Pau and Pays de l'Adour, 2009.

[KHA 13] KHADDOUR F., GREGOIRE D., PIJAUDIER-CABOT G., "Upscaling permeation properties in porous materials from pore size distributions", in PIJAUDIER-CABOT G., PEREIRA J.-M. (eds), *Geomechanics in CO_2 Storage Facilities,* ISTE Ltd., London and John Wiley & Sons, pp. 43–56, 2013.

[KHA 15] KHADDOUR F., GREGOIRE D., PIJAUDIER-CABOT G., "Capillary bundle model for the computation of the apparent permeability from pore size distributions", *European Journal of Environmental and Civil Engineering*, vol. 19, no. 2, pp. 168–183, 2015.

[KOR 07] KORB J.-P., "Microstructure and texture of cementitious porous materials", *Magnetic Resonance Imaging*, vol. 25, no. 4, pp. 466–469, 2007.

[KUR 06] KURUMISAWA K., TANAKA K., "Three-dimensional visualization of pore structure in hardened cement paste by the gallium intrusion technique", *Cement and Concrete Research*, vol. 36, no. 2, pp. 330–336, 2006.

[LAN 00] LANDIS E.N., NAGY E.N., "Three-dimensional work of fracture for mortar in compression", *Engineering Fracture Mechanics*, vol. 65, no. 2, pp. 223–234, 2000.

[LAN 10] LANDIS E.N., KEANEB D.T., "X-ray microtomography", *Materials Characterization*, vol. 61, no. 12, pp. 1305–1316, 2010.

[LEV 07] LEVITZ P., "Toolbox for 3D imaging and modeling of porous media: relationship with transport properties", *Cement and Concrete Research*, vol. 37, no. 3, pp. 351–359, 2007.

[LUR 11] LURA P., TRTIK P., MÜNCH B., "Validity of recent approaches for statistical nanoindentation of cement pastes", *Cement and Concrete Composites*, vol. 33, no. 4, pp. 457–465, 2011.

[MUN 09] MUNROE P.R., "The application of focused ion beam microscopy in the material sciences", *Materials Characterization*, vol. 60, no. 1, pp. 2–13, 2009.

[NAD 13] NADAH J., BIGNONNET F., DAVY C. *et al.*, "Microstructure and poro-mechanical performance of Haubourdin chalk", *International Journal of Rock Mechanics and Mining Sciences*, vol. 58, pp. 149–165, 2013.

[OLL 92] OLLIVIER J.P., MASSAT M., "Permeability and microstructure of concrete: a review of modeling", *Cement and Concrete Research*, vol. 22, pp. 503–514, 1992.

[PAT 12] PATURAL L., KORB J-P., GOVIN A. *et al.*, "Nuclear magnetic relaxation dispersion investigations of water retention mechanism by cellulose ethers in mortars", *Cement and Concrete Research*, vol. 42, no. 10, pp. 1371–1378, 2012.

[PIC 01] PICANDET V., Influence d'un endommagement mécanique sur la perméabilité et sur la diffusivité hydrique des bétons, PhD Thesis, University of Nantes, 2001.

[PIG 05] PIGNAT C., NAVI P., SCRIVENER K., "Simulation of cement paste microstructure hydration, pore space characterization and permeability determination", *Materials and Structures*, vol. 38, no. 4, pp. 459–466, 2005.

[PLA 01] PLASSAIS A., POMIÈS M-P., LEQUEUX N. *et al.*, "Micropore size analysis in hydrated cement paste by NMR", *Magnetic Resonance Imaging*, vol. 19, nos. 3–4, pp. 493–495, 2001.

[PRO 09] PROMENTILLA M.A.B., SUGIYAMA T., HITOMI T. *et al.*, "Quantification of tortuosity in hardened cement pastes using synchrotron-based X-ray computed microtomography", *Cement and Concrete Research*, vol. 39, no. 6, pp. 548–557, 2009.

[REI 92] REINHARDT H.W., GABER K., "From pore size distribution to an equivalent pore size of cement mortar", *Materials and Structures*, vol. 25, pp. 3–15, 1992.

[ROU 09] ROUGELOT T., SKOZYLAS F., BURLION N., "Water desorption and shrinkage in mortar and cement pastes: experimental study and poromechanical model", *Cement and Concrete Research*, vol. 39, no. 1, pp. 36–44, 2009.

[SCR 04] SCRIVENER K., "Backscattered electron imaging of cementitious microstructures: understanding and quantification", *Cement and Concrete Composites*, vol. 26, no. 8, pp. 935–945, 2004.

[SHI 89] SHI D., BROWN P.W., KURTZ S., *In Pore Structure and Permeability of Cementitious Materials*, Materials Research Society, Pittsburgh, pp. 23–34, 1989.

[SIN 04] SING K.S.W., "Characterization of porous materials: past, present and future", *Colloids and Surfaces A: Physicochemical and Engineering Aspects*, vol. 241, nos. 1–3, pp. 3–7, 14 July 2004.

[TOR 99] TORRENTI J-M., DIDRY O., OLLIVIER J-P. *et al.*, *La dégradation des bétons. Couplage fissuration – dégradation chimique*, Hermès, 1999.

[VAN 81] VAN BRAKEL J., MODRY S., SVATA M., "Mercury porosimetry: the state of the art", *Powder Technology*, vol. 29, pp. 1–12, 1981.

[VAN 91] VAN BREUGEL K., Simulation of hydration and formation of structure in hardening cement-based materials, PhD Thesis, Delft University of Technology, Delft, The Netherlands, 1991.

[VAN 95] VAN BREUGEL K., "Numerical simulation of hydration and microstructural development in hardening cement-based materials (I) theory", *Cement and Concrete Research*, vol. 25, no. 2, pp. 319–331, 2009.

[WAN 13] WANG B., FAURE P., THIÉRY M. *et al.*, "1H NMR relaxometry as an indicator of setting and water depletion during cement hydration", *Cement and Concrete Research*, vol. 45, pp. 1–14, 2013.

[WAR 81] WARDLAW N.C., MCKELLAR M., "Mercury porosimetry and the interpretation of pore geometry in sedimentary rocks and artificial models", *Powder Technology*, vol. 29, pp. 127–143, 1981.

[WIL 98] WILLIS K.L., ABELL A.B., LANGE D.A., "Image-based characterization of cement pore structure using wood's metal intrusion", *Cement and Concrete Research*, vol. 28, no. 12, pp. 1695–1705, 1998.

[YE 06] YE G., LURA P., VAN BREUGEL K., "Modeling of water permeability in cementitious materials", *Materials and Structures*, vol. 39, no. 9, pp. 877–885, 2006.

[ZHA 12] ZHANG M., HE Y., YE G. *et al.* "Computational investigation on mass diffusivity in Portland cement paste based on X-ray computed microtomography (μCT) image", *Construction and Building Materials*, vol. 27, no. 1, pp. 472–481, 2012.